Available online at www.sciencedirect.com
SCIENCE DIRECT®
Proceedings of the Combustion Institute 30 (2005) 2509–2517
Proceedings of the Combustion Institute
www.elsevier.com/locate/proci

Partial catalytic oxidation of methane to synthesis gas over rhodium: in situ Raman experiments and detailed simulations

Christoph Appel[a], John Mantzaras[a,*], Rolf Schaeren[a], Rolf Bombach[a], Andreas Inauen[a], Niclas Tylli[a], Markus Wolf[b], Timothy Griffin[b], Dieter Winkler[b], Richard Carroni[b]

[a] *Paul Scherrer Institute, Combustion Research, CH-5232 Villigen-PSI, Switzerland*
[b] *ALSTOM Power Technology Center, Segelhof, CH-5405 Baden-Daettwil, Switzerland*

Abstract

The partial catalytic oxidation of methane to synthesis gas over Rh/ZrO_2 was investigated experimentally and numerically at fuel-to-air equivalence ratios of 2.5 and 4.0 and pressures of 4 and 6 bar. Experiments were performed in an optically accessible, laboratory-scale, channel-flow catalytic reactor and involved in situ one-dimensional Raman measurements of major species (CH_4, O_2, H_2O, CO_2, H_2, CO, and N_2) concentrations across the reactor boundary layer. The numerical model included a two-dimensional elliptic code with elementary homogeneous (gaseous) and heterogeneous (catalytic) chemical reaction schemes. Homogeneous ignition experiments and numerical predictions have validated the employed gas-phase reaction mechanism and have further delineated the reactor extent over which the contribution of the homogeneous reaction pathway was negligible. Over the reactor extent where oxygen was still available, the employed heterogeneous reaction scheme provided good agreement with the measured species concentrations, overpredicting only to a small degree the partial over the total oxidation route. In the oxygen-depleted zones of the reactor, however, the heterogeneous scheme overpredicted to a greater degree the impact of steam reforming and water gas shift reactions, resulting in higher computed hydrogen yields at the reactor exit. Additional experiments and predictions were carried out in a sub-scale gas-turbine honeycomb reactor, at operating conditions leading to oxygen breakthrough. The predictions again favored the partial over the total oxidation route. A modified heterogeneous scheme was proposed that provided very good agreement with measurements in the honeycomb reactor and in the oxygen-rich zones of the laboratory-scale reactor. The hydrogen produced during partial oxidation was partly re-adsorbed on the catalyst leading to superadiabatic surface temperatures, thus exemplifying the importance of proper thermal management in commercial reactors.

Keywords: Partial catalytic oxidation of methane to synthesis gas over Rh; In situ Raman measurements

1. Introduction

The partial catalytic oxidation (PCO) of methane to synthesis gas has received increased

* Corresponding author. Fax: +41 56 310 21 99.
E-mail address: ioannis.mantzaras@psi.ch (J. Mantzaras).

1540-7489/$ - see front matter © 2004 The Combustion Institute. Published by Elsevier Inc. All rights reserved.
doi:10.1016/j.proci.2004.08.055

attention in many industrial applications such as chemical synthesis, fuel cells and, recently, gas-turbines of power generation systems. The adopted approach in gas-turbines involves the formation of a fuel-rich premixture (via mixing of the entire fuel stream with part of the air stream), which is partially oxidized in a catalytic reactor; the hot combustion products (synthesis gas, total oxidation products, and unburned reactants) are further mixed with the bypassed air and stabilize a post-catalyst gaseous flame [1]. This approach has two advantages in comparison to the conventional, fuel-lean catalytically stabilized combustion (CST) [2]; the first is the lower light-off temperature of the PCO reactor, the reason being that noble metals are more active in the oxidation of fuel-rich rather than of fuel-lean hydrocarbon/air mixtures [3], and the second is the enhanced stability of the ensuing flame due to the highly reactive H_2 contained in the synthesis gas. Knowledge of the heterogeneous (catalytic) and homogeneous (gas-phase) kinetics of methane is crucial for the progress of PCO; validated hetero/homogeneous reaction schemes can be further used in multidimensional CFD codes for reactor design.

Elementary heterogeneous reaction schemes for PCO of methane over Pt and Rh were developed in the last years [4–6]. Recently [7,8], we introduced the methodology of in situ spatially resolved Raman measurements of major species concentrations over the catalyst boundary layer as a direct way to assess the catalytic reactivity at realistic operating conditions: Appel et al. [7] and Reinke et al. [8] investigated the complete oxidation over Pt of fuel-lean H_2/air mixtures at $p = 1$ bar and fuel-lean CH_4/air mixtures at $4 \leqslant p \leqslant 16$ bar, respectively. In the present study, we apply the aforesaid methodology to investigate the partial oxidation of fuel-rich CH_4/air mixtures over a supported Rh catalyst, with the main objective of assessing the performance of the heterogeneous scheme in terms of CH_4 conversion and synthesis gas production. Additional objectives were to examine other heterogeneously catalyzed processes (such as steam reforming of CH_4) and to address PCO reactor performance issues. Experiments were performed in a laboratory-scale reactor and in a sub-scale gas-turbine burner. The numerical predictions included a 2D elliptic CFD model with elementary heterogeneous and homogeneous reaction schemes and detailed transport.

2. Experimental

2.1. High-pressure test-rigs and catalyst preparation

The laboratory-scale test-rig (Fig. 1) consisted of a rectangular, optically accessible reactor, which formed a liner inside a high-pressure cylindrical

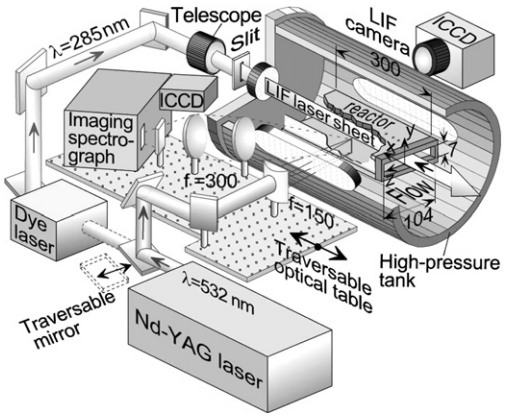

Fig. 1. Schematic of the test-rig and the Raman/LIF set-up.

tank [9]. The reactor comprised of two horizontal, non-porous Si[SiC] ceramic plates (300 mm long, 110 mm wide, 9 mm thick, placed 7 mm apart) and two 3-mm-thick vertical quartz windows [7]. The inner Si[SiC] surfaces were coated with Rh/ZrO_2 (1% wt. Rh). The surface temperature along the x–y symmetry plane was measured by S-type thermocouples embedded 0.9 mm beneath the catalyst, through holes made from the outer Si[SiC] surfaces. Two resistive heaters positioned above the outer Si[SiC] surfaces controlled the ceramic plate temperatures. Preheated air was mixed with CH_4 and then directed into the reactor through a 50-mm-long inert rectangular honeycomb section. A thermocouple positioned at the downstream end of the honeycomb monitored the reactor inlet temperature. The high-pressure tank was equipped with two 350-mm-long and 35-mm-thick quartz windows that provided optical access from both reactor sides. Two additional quartz windows, one located at the rear flange of the high-pressure tank and the other (not shown in Fig. 1) at the reactor exhaust, provided a further streamwise optical access.

The sub-scale gas-turbine test rig consisted of a honeycomb reactor (16 mm in diameter, 50 mm long) fabricated out of 150 μm thick corrugated FeCr-alloy foils; the hydraulic diameter of each individual channel being 1.2 mm. The FeCr foils were coated with the same Rh/ZrO_2 catalyst as the Si[SiC] plates of the laboratory-scale reactor. Due to thermal management considerations (as discussed later on), only every second channel was coated, creating an alternately coated honeycomb structure. Details of the test-rig have been provided elsewhere [10]. The reactor inlet and outlet temperatures were measured with thermocouples and the outlet composition with a two-column gas-chromatograph.

The catalyst was prepared by incipient wetness impregnation of the ZrO_2 support with a

$Rh(NO_3)_3$ solution. The impregnated catalyst powder was calcined at 600 °C for 5 h. A slurry prepared from the powder and a solvent mixture was sprayed on the Si[SiC] plates and the FeCr foils, yielding a 30-μm-thick coating. The coated Si[SiC] plates and the FeCr foils were further calcined at 600 °C for 1 h. The total and active areas were measured on the FeCr-coated foils before and after the combustion tests with BET (N_2 physisorption) and CO chemisorption, respectively. The measured active-to-total area ratio was 3.8% on the fresh and 1.4% on the combusted samples; the latter value corresponding to a metal dispersion (surface-to-bulk Rh) of 5.9% and maintained during subsequent runs. The surface composition of the FeCr-coated foils was measured with X-ray photoelectron spectroscopy (XPS); the post-combustion analysis indicated that Fe or Cr did not diffuse to the surface.

2.2. Laser diagnostics

The Raman experiments could also be used for the detection of a strong gaseous flame. However, since Raman data were acquired at discrete axial positions, a more accurate mapping of the potentially established flames was desirable with planar OH-LIF. The Raman/LIF set-up is depicted in Fig. 1. A traversable mirror directed the 532-nm beam of a frequency-doubled Nd:YAG pulsed laser (Quantel YG781C20, 210 mJ pulse energy, 14 ns pulse duration) to the Raman- or to the LIF-set-up. In the Raman tests, the 532-nm beam was focused through the tank and reactor sidewindows into a vertical line (~0.3 mm thick) by an $f = 150$ mm cylindrical lens. The focal line spanned the entire 7-mm transverse gap and was laterally offset ($z = 15$ mm) to increase the collection angle and minimize thermal beam steering, as in [7]. Two $f = 300$ mm lenses collected the scattered light, at 40° with respect to the sending optical path, and focused it to the entrance slit of a 25-cm imaging spectrograph (Chromex-250i). The dispersed light was recorded on an intensified CCD camera (Princeton Instruments MAX:1024HQ, 1024×254 pixels). To increase the spatial resolution, only the lower part of the channel was recorded on the CCD. The 630×254 pixels of the recorded images corresponded to wavelength and physical distance, respectively. The 3.5-mm half-height was resolved with 200 pixels, which were further binned to 84 pixels. A holographic notch filter (Kaiser optical systems HNPF) was placed before the spectrograph slit to attenuate the Rayleigh signal and the scattered stray laser light. The spectral dispersion on the CCD camera extended up to 4500 cm^{-1}, allowing observation of all major species; the Raman shift ranged from 1388 cm^{-1} (CO_2) to 4155 cm^{-1} (H_2). An average of 3000 images was used to improve the signal-to-noise ratio. The effective Raman cross-sections, which included transmission efficiencies, were evaluated by recording the signals of several pressurized N_2/H_2- and CO_2-containing mixtures, air, and the actual fuel/air mixture; those tests were also used to quantify the cross-talk between the CO_2/O_2 and the CO/N_2 signals. Spectroscopic data for the CH_4, the H_2O/CO_2, and the CO Raman cross-sections were obtained from [11], [12], and [13], respectively. Measurements were acquired every 20 mm over the extent $12 \text{ mm} \leqslant x \leqslant 172$ mm by traversing axially an optical table that supported the sending and collecting optics. Raman data points closer than 0.4 mm to the wall were discarded due to low signal-to-noise ratio.

In the LIF tests, the 532-nm radiation pumped a tunable dye laser (Quantel TDL50). Its frequency-doubled radiation (285 nm) was transformed into a laser sheet (by a cylindrical lens and a 1-mm slit mask) that propagated counterflow, along the x–y symmetry plane (Fig. 1). The fluorescence of both (1–1) and (0–0) transitions was collected at 90° with an intensified CCD camera (LaVision FlameStar 2F, 576×384 pixels); details of the LIF set-up have been provided elsewhere [7,9].

3. Numerical

Simulations were carried out with an elliptic 2D CFD code [7,14]. The heterogeneous scheme of Deutschmann et al. [6] (38 reactions, 12 surface, and 6 gaseous species) and the gaseous $C_2/H/O$ scheme of Warnatz et al. [15] (164 reversible reactions and 34 species, with appropriate pressure dependencies for 6 reactions) were employed. The CHEMKIN database provided the gas-phase thermochemical [16] and transport [17] properties. Mixture-average diffusion, including thermal diffusion [17], was used in the species transport. Gaseous and surface chemical reaction rates were evaluated with CHEMKIN [18] and Surface-CHEMKIN [19], respectively. Surface thermochemical data were taken from [6].

An orthogonally staggered grid of 480×84 grid points (in x and y, respectively, over the entire 300×7 mm^2 domain) was used. The inlet boundary conditions were uniform profiles for the temperature, the axial velocity, and the species mass fractions. Fitted curves through the individual thermocouple measurements provided the bottom and top wall temperature profiles, which were used as energy boundary conditions at $y = 0$ and 7 mm, respectively. No-slip conditions for both velocity components were applied at the walls and zero-Neumann conditions at the reactor outlet.

The previous code was also used to simulate an individual catalytic channel of the honeycomb; an axisymmetric model was adopted, with 100×24 grid points in the axial (50 mm) and radial

(0.6 mm) directions, respectively. For the unknown catalyst temperature, the surface energy equation was additionally solved. Heat conduction in the solid substrate, thermal radiation exchange between the hot surfaces, and the alternately coated nature of the reactor were all accounted for: details have been provided in a recent fuel-lean CST study [10].

4. Results and discussion

Four laminar-flow cases were investigated (see Table 1), the first three referring to the optically accessible reactor and the fourth one to the commercial honeycomb. The underlying combustion processes are first elaborated with the detailed in-channel measurements (Cases 1–3). Comparisons between Raman-measured and numerically predicted transverse species profiles are illustrated in Figs. 2–4; for clarity, up to 18 measuring points are shown over the exploitable range $0 \leqslant y \leqslant 3.1$ mm (in the notation of Figs. 2–4, $y = 0$ and 3.5 mm denote the channel center and lower wall, respectively). The measured lower-wall surface temperatures (Fig. 5) did not exceed 1150 K, and they differed by less than ±15 K from the upper-wall temperatures The measurement uncertainty in the surface temperatures was better than 4 K (see [7]). The moderate temperatures and high pressures of the present study favored high Raman signals. Therefore, the species measurement accuracy was estimated to ±3% for volumetric compositions ⩾10%, and ±10% for volumetric compositions as low as 0.5%; concentrations lower than 0.5% per vol. could not be accurately resolved. Given the Raman profiles of Figs. 2–4, the C/H/O element balances were reproduced within 5% along the channel. The average (over y) streamwise species profiles of Fig. 5 indicated that complete O_2 consumption was practically reached in Cases 2 and 3 at $x < 172$ mm, thus allowing for a detailed investigation of not only PCO, but also of other heterogeneously catalyzed processes (such as steam reforming) that dominated the O_2-depleted zones.

To evaluate the catalytic processes, a parallel assessment of the gaseous reaction pathway was also necessary. A strong flame was established in Case 3, as evidenced by an abrupt drop in the measured CH_4 and O_2 (Figs. 4A and B), between

Table 1
Experimental conditions[a]

Case	p (bar)	φ	T_{IN} (K)	U_{IN} (m/s)	Re_{IN}
1	4.0	4.0	395	0.30	642
2	6.0	4.0	385	0.19	652
3	6.0	2.5	419	0.21	612
4	5.7	4.0	673	13.2	1374

[a] Pressure, equivalence ratio, inlet temperature, velocity, and Reynolds number.

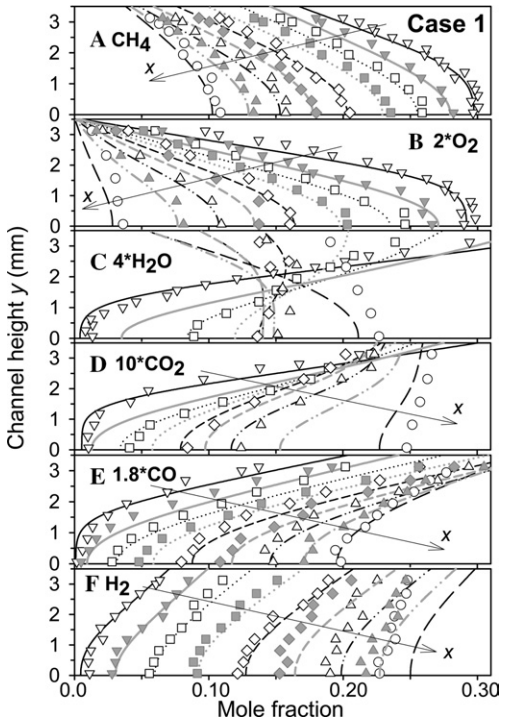

Fig. 2. Measured (symbols) and predicted (lines) species profiles, Case 1: $x = 12$ mm (black solid line, open lower-triangles), $x = 32$ mm (gray solid, filled lower-triangles), $x = 52$ mm (black dotted, open squares), $x = 72$ mm (gray dotted, filled squares), $x = 92$ mm (black short-dashed, open diamonds), $x = 112$ mm (gray short-dashed, filled diamonds), $x = 132$ mm (black double-dotted-dashed, open upper-triangles), $x = 152$ mm (gray double-dotted-dashed, filled upper-triangles), and $x = 172$ mm (black long-dashed, open circles). For clarity, in (C) and (D) every second measured profile is shown.

$x = 72$ mm (filled squares) and 92 mm (open diamonds). The predictions indicated a somewhat later ignition, between $x = 92$ and 112 mm. The small mismatch could be attributed to the gaseous pathway itself and/or to the small differences between the measured and predicted heterogeneous processes observed upstream of the flame. The computed 2D maps of OH and temperature for Case 3 (Fig. 6) indicated the formation of a well-defined flame front at $x \approx 98$ mm. The OH-LIF measurements, however, did not capture this flame. Even though the peak flame temperature reached 1580 K (Fig. 6B), the maximum predicted OH levels were only 0.9 ppm (Fig. 6A) due to the significant upstream depletion of O_2 (Fig. 5C). Sub-ppm OH levels were, in turn, not amenable for planar LIF. It is further noted that the flame was stabilized in the channel core, away from the wall (Fig. 6A), due to the catalytic depletion of O_2 in the near-wall zone (Fig. 4B). In Cases 1 and 2, very weak flames were predicted at

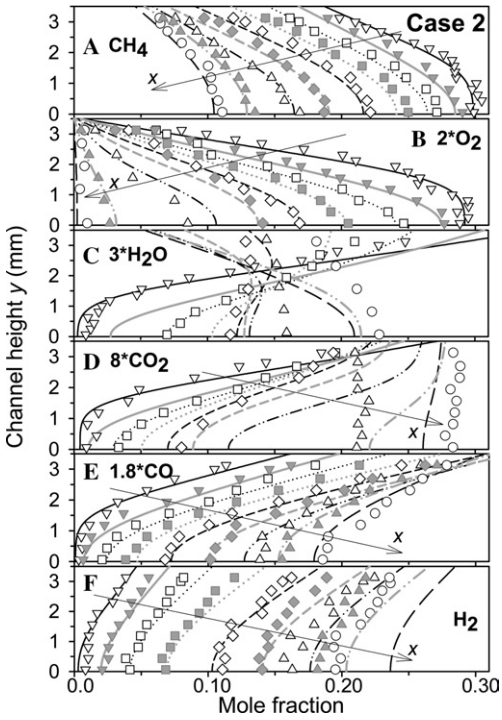

Fig. 3. Measured and predicted species profiles, Case 2. The notation follows Fig. 2.

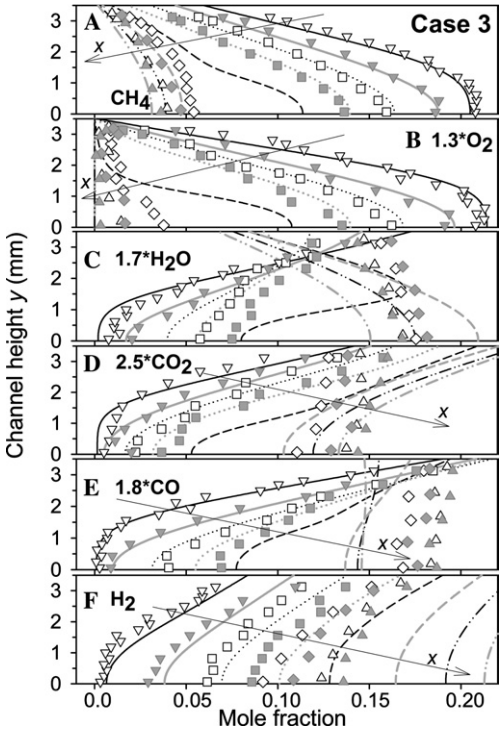

Fig. 4. Measured and predicted species profiles ($x \leqslant 152$ mm), Case 3. The notation follows Fig. 2.

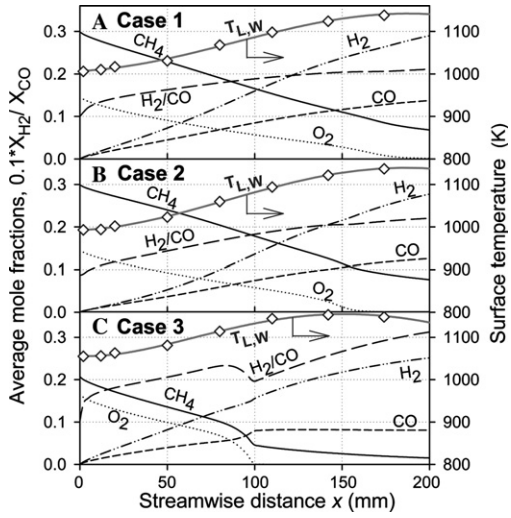

Fig. 5. Streamwise profiles of the lower-wall temperatures (solid gray-lines), fitted through the measurements (diamonds). The predicted y-averaged profiles of mole fractions are shown with black lines: CH_4 (solid), O_2 (dotted), CO (dashed), H_2 (double-dotted-dashed), and H_2/CO (long-dashed).

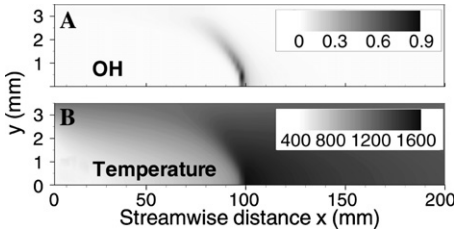

Fig. 6. Predicted OH (ppm-vol.) and temperature (K) distributions, Case 3. The wall is at $y = 3.5$ mm.

$x \approx 170$ and 150 mm, respectively (see Figs. 7A and B)), which were not captured either by LIF or Raman measurements.

Notwithstanding the small overprediction in the flame position of Case 3, the scheme of Warnatz appeared to be realistic in describing gaseous combustion; it was, therefore, used to delineate the reactor extent with minimal gas-phase participation. The production rates of Fig. 7 indicated that the gaseous pathway was negligible in Cases 1, 2, and 3 for $x \leqslant 90$ mm, $x \leqslant 70$ mm, and $x \leqslant 40$ mm, respectively. Over those extents, which are further denoted as PCO zones, the predicted profiles of Figs. 2–4 remained unaffected by the inclusion of gaseous chemistry. Moreover, the aforesaid axial positions roughly delineated the onset of significant heterogeneously catalyzed steam reforming, as manifested by the sign change (from positive to negative) of the H_2O catalytic production rates in Fig. 7. Since steam reforming

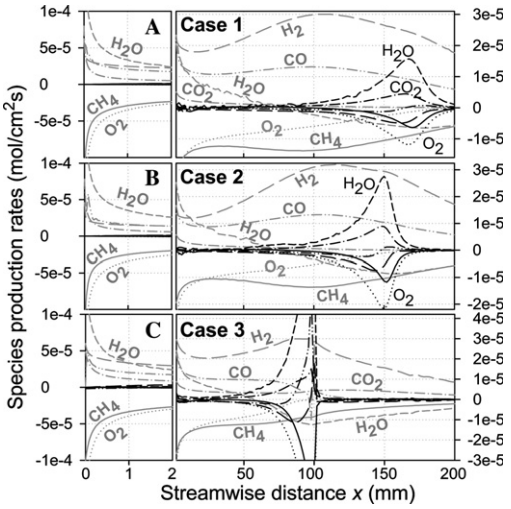

Fig. 7. Predicted species production rates. Gray lines indicate the catalytic and black the gaseous rates (the latter integrated over y): CH_4 (solid), O_2 (dotted), H_2O (short-dashed), CO_2 (dotted-dashed), H_2 (long-dashed), and CO (double-dotted-dashed). For clarity, the initial 2 mm is expanded.

was a source of discrepancy between the experiments and predictions (as addressed later on), the exclusion of this process was desirable in the ensuing PCO analysis. Over the PCO zones (corresponding to the first 4, 3, and 2 profiles in Figs. 2–4, respectively), there was always an O_2 breakthrough (see Fig. 5), and the agreement between predicted and measured species concentrations was particularly good (Figs. 2–4). There was a small but systematic underprediction of CH_4 by up to 5%; however, these differences were within the measuring uncertainty. At the same time, the CO and CO_2 levels were slightly overpredicted and underpredicted, respectively; an even smaller overprediction/underprediction of the H_2/H_2O levels was also apparent. Therefore, it appeared that the heterogeneous reaction scheme slightly favored the partial over the total oxidation route. The partial oxidation route suggested a molar destruction ratio $CH_4{:}O_2$ of 2:1, according to $2CH_4 + O_2 \rightarrow 4H_2 + 2CO$. In the first 2 mm, however, the catalytic destruction rate of O_2 exceeded that of CH_4 (Fig. 7), indicating a strong contribution of the total oxidation route $CH_4 + 2O_2 \rightarrow 2H_2O + CO_2$. Farther downstream, the destruction rate of CH_4 overtook that of O_2, such that the molar ratio H_2/CO approached 2 at the end of the PCO zones (Fig. 5). The presence of an initially strong total oxidation was associated with very steep transverse gradients of the H_2O and CO_2 at the wall (see, for example, the first two profiles in Figs. 2C and D, 3C and D). Although the total oxidation was usually accompanied by the formation of hot-spots [20], this was not evident in the measured temperature profiles of Fig. 5 due to the large thermal inertia of the catalytic plates and their direct contact with the cooler reactor frame. To further improve the agreement between the experiment and predictions, two surface reactions were modified. The modifications were aided by a sensitivity analysis of the reaction scheme. The pre-exponential of $CO(s) + O(s) \rightarrow CO_2(s)$ and the methane desorption $CH_4(s) \rightarrow CH_4 + Rh(s)$ ((s) denotes a surface species) was increased by a factor of 1.5 and 2, respectively. The change in the first reaction reduced/increased the predicted CO/CO_2 levels, while the change in the second reaction reduced the CH_4 consumption; their combined effect was an improved agreement (within ±2%) with the measured CO/CO_2 and CH_4 profiles of Figs. 2–4. The aforesaid changes also slightly decreased (increased) the predicted H_2 (H_2O) levels, again improving their agreement with the measurements; in addition, they had a negligible impact on the predicted flame positions.

The processes downstream of the PCO zones are further discussed. In the O_2-depleted zones of Case 3 ($x > 100$ mm), the predictions indicated an on-going catalytic consumption of CH_4 (see Fig. 7C and also the last three computed profiles of Fig. 4A), a significant catalytic consumption/production of H_2O/H_2, respectively, a catalytic production of CO_2, and a decreasing with axial distance minute production of CO (Fig. 7C and 4). This was due to the heterogeneously catalyzed endothermic steam reforming, $CH_4 + H_2O \rightarrow CO + 3H_2$. However, the H_2/CH_4 production/destruction ratio exceeded 3 (it ranged from 3.3 to 4.1 over $x > 100$ mm, Fig. 7C) due to an additional heterogeneously catalyzed step, the exothermic water gas shift reaction $CO + H_2O \rightarrow CO_2 + H_2$. This step consumed the CO produced via steam reforming (resulting in the nearly zero catalytic CO production rate of Fig. 7C and in the increasing with axial distance H_2/CO ratio of Fig. 5C), and resulted in the catalytic production of CO_2. The capacity of the heterogeneous scheme to accommodate steam reforming and water gas-shift reactions was verified with additional computations for Cases 1–3, where CH_4/H_2O and CO/H_2O replaced the mixtures of Table 1. The data of Fig. 4 have also indicated an on-going CH_4 conversion in the O_2-depleted zones; however, the catalytic scheme significantly overpredicted the impact of steam reforming and water gas-shift reactions. The measured H_2O at $x > 100$ mm (last three profiles in Fig. 4C) was nearly flat having a considerably weaker gradient at the wall compared to the predicted one, indicating only a small H_2O adsorption; the measured CO_2 desorption was also smaller (Fig. 4D). Hence, the steam reforming and/or water gas shift reactions proceeded at a pace slower than that of

the predictions, as also supported by a considerably lower measured H_2 in Case 3 at large x (Fig. 4F).

In Cases 1 and 2, where O_2 was consumed farther downstream (Figs. 5A and B), PCO occurred parallel to steam reforming (as shown in Figs. 7A and B) by a change in the sign of the catalytic H_2O rates well before O_2 depletion); water gas shift reactions were not present in the more fuel-rich Cases 1 and 2. Again, the measured H_2O adsorption rate at $x = 172$ mm (circles in Figs. 2C and 3C) was weaker compared to the predicted one, and the H_2 levels were overpredicted (Fig. 2F and 3F). The surface coverage in Cases 1 and 2 (Fig. 8) shifted from free-sites and CO(s) to C(s) after significant O_2 depletion. One possible reason for the differences between experiments and predictions in the O_2-deprived zones could be the underprediction of C(s). The extension of the original catalytic scheme to capture steam reforming/water gas-shift reactions was highly desirable for many practical systems [1] that utilized CH_4/O_2 mixtures highly diluted with H_2O/CO_2 exhaust (up to 60% H_2O and 30% CO_2, per vol.).

Comparisons between measured and predicted exit compositions and temperatures for Case 4, referring to the active channels of the commercial honeycomb, are given in Table 2. The predictions refer to both the original and modified (in the two aforementioned reactions) schemes of Deutschmann. In Case 4, which had O_2 breakthrough and a shorter residence time compared to Cases 1–3, the computations indicated that the gaseous pathway was negligible. The original catalytic scheme overpredicted the partial oxidation products (and

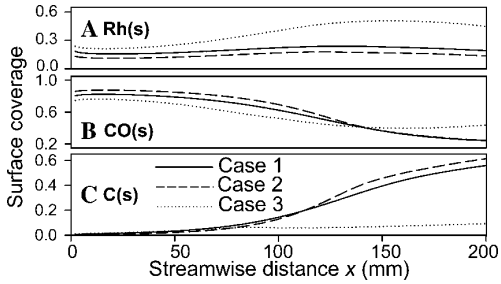

Fig. 8. Major surface species coverage, Cases 1–3.

Table 2
Measurements and simulations for Case 4[a]

	T_{OUT} (K)	CH_4	O_2	H_2O	CO_2	CO	H_2
Meas.	988	22.3	5.6	8.9	2.1	3.9	3.9
Sim.(a)	967	20.8	5.9	7.9	1.5	5.6	6.6
Sim.(b)	994	22.3	6.0	7.8	2.5	3.5	4.4

[a] Volumetric exit composition (%). Reaction scheme: (a) original, (b) modified.

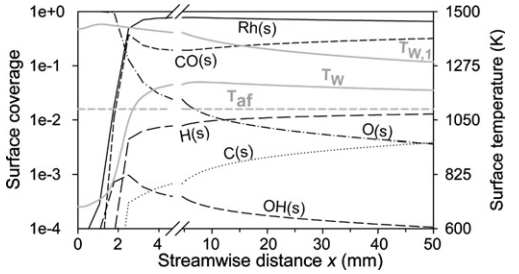

Fig. 9. Predicted surface temperature (T_W) and coverage for Case 4; $T_{W,1}$ is the temperature of a fully coated honeycomb.

hence underpredicted the exit temperature) as well as the CH_4 conversion, consistent with the previous in-channel investigation. The modified reaction scheme gave a better agreement to the measurements. It is emphasized that although the exit H_2 levels were low in both predictions, their differences could be important for the stabilization of the ensuing flame [1]. The surface coverage and temperature profiles of Fig. 9 (modified reaction scheme) indicated that light-off occurred at $x \approx 3$ mm, where the dominant coverage shifted from O(s) to Rh(s). The surface temperature T_W peaked shortly after light-off, indicative of total oxidation at the reactor entry. Additional computations with a fully coated honeycomb provided the temperature profile $T_{W,1}$ (Fig. 9). Both T_W and $T_{W,1}$ exceeded the adiabatic flame temperature, T_{af}, of the incoming mixture by 128 and 350 K, respectively; the latter temperature overshoot could cause catalyst meltdown. The reason for this phenomenon was the re-adsorption of the PCO-produced hydrogen on the catalyst, leading to the well-known superadiabatic effects of diffusionally imbalanced fuels with Lewis numbers less than unity [7].

5. Conclusions

The partial catalytic oxidation (PCO) of methane to synthesis gas over Rh was investigated with in situ experiments and numerical predictions. The employed heterogeneous scheme slightly overpredicted the partial over the total oxidation route in the oxygen-containing zones, and significantly overpredicted the steam reforming and water gas shift reactions in the oxygen-depleted zones. A modification of two surface reactions improved the PCO predictions in the oxygen-containing zones of the laboratory-scale reactor and further provided good agreement to the measured exit compositions and temperature in a commercial honeycomb reactor. It was shown that the design of PCO reactors should carefully consider the superadiabatic temperatures attained due to re-adsorption of H_2.

Acknowledgments

Support was provided by the Swiss Federal Office of Energy (BFE) and Swiss Federal Office of Education and Science (BBW). We thank Ms. F. Geiger and Dr. F. Raimondi for the BET and XPS, and Ms. S. Eriksson for the catalyst preparation.

References

[1] M. Wolf, C. Appel, J. Mantzaras, T. Griffin, R. Carroni, in: *Seventh International Conference for a Clean Environment*, Lisbon, Portugal, July 7–10, 2003.
[2] R. Carroni, V. Schmidt, T. Griffin, *Catal. Today* 75 (2002) 287–295.
[3] G. Veser, M. Ziauddin, L.D. Schmidt, *Catal. Today* 47 (1999) 219–228.
[4] D.A. Hickman, L.D. Schmidt, *AIChE* 39 (7) (1993) 1164–1177.
[5] P. Aghalayam, Y.K. Park, N. Fernandes, V. Papavassiliou, A.B. Mhadeshwar, D.G. Vlachos, *J. Catal.* 213 (2003) 23–38.
[6] R. Schwiedernoch, S. Tischer, C. Correa, O. Deutschmann, *Chem. Eng. Sci.* 58 (2003) 633–642.
[7] C. Appel, J. Mantzaras, R. Schaeren, R. Bombach, A. Inauen, B. Kaeppeli, B. Hemmerling, A. Stampanoni, *Combust. Flame* 128 (2002) 340–368.
[8] M. Reinke, J. Mantzaras, R. Schaeren, R. Bombach, A. Inauen, S. Schenker, *Combust. Flame* 136 (2004) 217–240.
[9] M. Reinke, J. Mantzaras, R. Schaeren, R. Bombach, W. Kreutner, A. Inauen, *Proc. Combust. Inst.* 29 (2002) 1021–1030.
[10] R. Carroni, T. Griffin, J. Mantzaras, M. Reinke, *Catal. Today* 83 (2003) 157–170.
[11] B. Steiner, Ph.D. Thesis, The University of Stuttgart, 2002.
[12] S. Eisenberg, Diploma Thesis, Max Planck Institut, Göttingen, 1995.
[13] H.W. Schroetter, in: W. Kiefer, D.A. Long (Eds.), *Non-Linear Raman Spectroscopy and its Chemical Applications.* D. Reidel, Dordrecht, Netherlands, 1982.
[14] U. Dogwiler, P. Benz, J. Mantzaras, *Combust. Flame* 116 (1999) 243–258.
[15] J. Warnatz, R.W. Dibble, U. Maas, *Combustion, Physical and Chemical Fundamentals, Modeling and Simulation.* Springer-Verlag, New York, 1996, p. 69.
[16] R.J. Kee, F.M. Rupley, J.A. Miller, *The Chemkin Thermodynamic Data Base*, Report No. SAND87-8215B, Sandia National Laboratories, 1996.
[17] R.J. Kee, G. Dixon-Lewis, J. Warnatz, M.E. Coltrin, J.A. Miller, *A Fortran Computer Code Package for the Evaluation of Gas-phase Multicomponent Transport Properties*, Report No. SAND86-8246, Sandia National Laboratories, 1996.
[18] R.J. Kee, F.M. Rupley, J.A. Miller, *Chemkin II: A Fortran Chemical Kinetics Package for the Analysis of Gas-phase Chemical Kinetics*, Report No. SAND89-8009B, Sandia National Laboratories, 1996.
[19] M.E. Coltrin, R.J. Kee, F.M. Rupley, *Surface Chemkin: A Fortran Package for Analyzing Heterogeneous Chemical Kinetics at the Solid Surface-gas Phase Interface*, Report SAND90-8003C, Sandia National Laboratories, 1996.
[20] O. Deutschmann, L.D. Schmidt, *AIChe* 44 (11) (1998) 2465–2477.

Comments

Firooz Rasouli, Philip Morris USA. In the Rh/ZrO_2 system is ZrO_2 acting as support? Do you have any ceria (CeO_2) in the catalytic system?

Reply. The Rh/ZrO_2 catalyst of this investigation did not contain any ceria. CO chemisorption tests indicated that there was a drop in Rh dispersion (surface-to-bulk ratio) from 22.9% (fresh sample) to 5.9% (sample after combustion). This was due to loss of the high-surface-area tetragonal phase: surface Raman experiments have further showed that the morphology of the surface prior to combustion consisted of both monoclinic and tetragonal phases, whereas after combustion only the monoclinic phase was present. Tests with CeO_2-doped Rh/ZrO_2 catalysts (not presented in this paper) have shown that CeO_2 is beneficial as it stabilizes the high-surface-area tetragonal phase.

•

Greg Jackson, University of Maryland, USA. Can you describe the physical structure of the Rh/ZrO_2 coating? What are the possibilities of intraphase diffusion of the porous coating influencing kinetic rates?

Reply. For the structure of the Rh/ZrO_2 coating, please see the response in the first question. The Rh/ZrO_2 coating was applied on non-porous Si[SiC] ceramic plates and on non-porous FeCr metal foils. The Rh/ZrO_2 catalyst had a thickness of only 20-30 microns: therefore, intraphase diffusion limitations are not likely to be of importance. There have been only special cases of catalyst/fuel systems where appreciable intraphase diffusion limitations were reported even for coatings as thin as 30 microns [1]: however, those cases do not appear relevant to the present study.

Reference

[1] R.E. Hayes, S.T. Kolaczkowski, *Chem. Eng. Science* 49 (21) (1994) 3587–3599.

•

Serguei Nester, GTI, USA. What is durability of the catalyst? How long do you expect it to work?

Reply. The present work is an activity and not a thermal stability investigation. Catalysts with enhanced thermal stability for gas-turbine applications would require appropriate modifications in their chemical composition as to assure good adhesion of the coating to the FeCr surface. In addition, additives such as those described in the first question may be relevant to practical systems.

•

J.Y. Chen, U.C. Berkeley, USA. 1. Will the increase in flow rate affect the heat transfer to the uncoated channel? 2. Is there NO_x produced in the gas phase?

Reply. 1. The flow rate (and hence the reactor residence time) determines the extent of the total and partial oxidation routes and, therefore, controls the surface temperature and the heat transfer to the uncoated channel. Short residence times (high flow rates) lead to sufficient oxygen levels throughout the reactor that, in turn, favor total oxidation with the associated high surface temperatures (Fig. 9). Longer residence times favor the partial oxidation and the endothermic steam reforming, the latter moderating the surface temperatures.

If the previous chemical effects originating from the presence of different reaction pathways are neglected and only one dominant pathway is considered, the alternately-coated system itself is not particularly flexible in controlling the heat transfer and hence the surface temperatures. Since the mass-flows in both active and inactive channels are roughly the same, a single catalytic reaction with a given exothermicity will lead to the same surface temperature irrespective of flow-rate magnitude (neglecting finite-rate surface chemistry at very high flow rates and differences in heat capacity and thermal conductivity between the unreacted gaseous mixtures in the uncoated channels and the partially reacted ones in the coated channels).

Finally, an additional factor that has to be considered is that an increased flow rate can move the surface reactions towards the kinetically controlled regime with a resulting lower heat release on the catalytically active surface and hence lower heat transfer to the uncoated channel.

2. In the subscale gas-turbine reactor (Case 4) oxygen is available over the entire reactor length and could potentially initiate NO_x chemistry: however, the gas temperatures are quite low (< 1200 K) and the residence times are very short (< 4 ms) for NO_x chemistry to be of importance.